J Adv Ceram

Research Article

Cross-scale structural engineering of MOF-derived Co_xNi_y@C nanorods with controllable electromagnetic response behavior for broadband electromagnetic wave absorption

Bo Huang[1], Fang Ye[1,✉], Jingwen Deng[1], Jingchao Wang[2], Chen Li[1], Yuchen Cao[1], Wenjing Zhang[1], Xiaomeng Fan[1]

Cite this article: Huang B, Ye F, Deng J, et al. *J Adv Ceram* 2026, **15**(2): 9221224. https://doi.org/10.26599/JAC.2025.9221224

ABSTRACT: Metal–organic framework (MOF) derivatives employed as electromagnetic wave (EMW) absorption materials have gained considerable attention because of their plentiful coordination components and diverse nanomicrostructures. However, achieving broadband EMW absorption solely through nanoscale structural design remains challenging. Herein, a cross-scale structural engineering strategy is proposed to address this limitation. At the nanomicroscale, MOF-derived Co_xNi_y@C nanorods were fabricated via a solvothermal and pyrolysis process. Systematic manipulation of the built-in electric field (BIEF) heterointerface achieved through adjusting the Co/Ni atomic ratio significantly promotes electron-directed migration, alters the spatial charge distribution, and ultimately enhances the polarization relaxation and magnetic resonance effects, resulting in superior EMW absorption performance (the effective absorption bandwidth of Co_2Ni@C is 4.9 GHz at 1.75 mm). The geometric configuration of the electromagnetic metastructures was subsequently optimized via CST software. Through cross-scale structural design, the simulated gradient honeycomb structure metamaterial composed of Co_2Ni@C achieves multiband compatibility, and the EAB reaches 38 GHz (covering 2–40 GHz) with a total thickness of 15 mm. This research elucidates the BIEF loss mechanism of MOF-derived Co_xNi_y@C composites by rationally controlling the Co/Ni atomic ratio and provides novel insights into the structural design of electromagnetic nanomaterials.

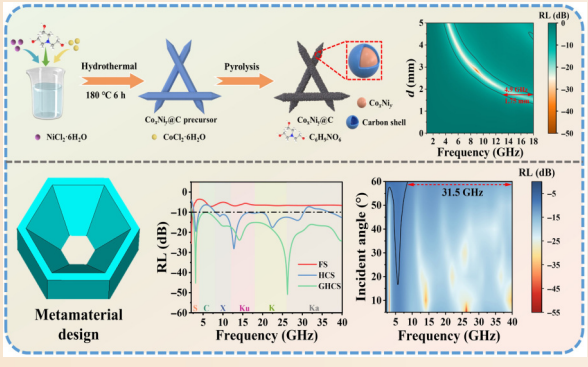

KEYWORDS: metal–organic framework derivatives; Co_xNi_y@C nanorods; structure engineering; electromagnetic synergistic; electromagnetic wave absorption

1 Introduction

With the booming development of fifth-generation communication technology (5G) and the miniaturization of electronic devices operating in the gigahertz (GHz) frequency band, electromagnetic wave (EMW) pollution has emerged as a critical global challenge, threatening information security, human health, and the stability of precision equipment [1–4]. EMW absorption materials, which can effectively convert EMW into heat energy without secondary pollution, have become a hot research topic in both civilian and military applications [5–7]. Conventional EMW absorption materials are constrained by high density and narrow absorption bandwidths, failing to achieve the urgent requirements for next-generation absorbers characterized by "lightweight, thinness, broad bandwidth, and strong absorption" [8–11]. To achieve ideal EMW absorption performance, numerous preparation strategies have been developed, including precise component design (such as carbon materials, MXenes, ferrites, and magnetic alloys) and diverse microstructure constructions (e.g., rod-like, cubic, flake-like, and foam architectures) [12–14]. Studies have shown that composites incorporating dielectric and magnetic components can synergistically satisfy impedance matching and attenuation requirements [15–17]. Therefore, the construction of high-performance EMW absorption materials with strong electromagnetic coupling has become a key research focus [18–20].

Metal-organic frameworks (MOFs) have become attractive candidates for EMW absorption materials because of their large specific surface area, designable pore structure, and

[1] Science and Technology on Thermostructural Composite Materials Laboratory, Northwestern Polytechnical University, Xi'an 710072, China. [2] State Key Laboratory of Solidification Processing, Northwestern Polytechnical University, Xi'an 710072, China.

✉ Corresponding author. E-mail: yefang511@nwpu.edu.cn

Received: September 26, 2025; Revised: November 16, 2025; Accepted: November 28, 2025

morphology/compositional diversity [21–23]. By pyrolyzing the MOF precursor, a hierarchical structure with metal nanoparticles embedded in the carbon matrix can be obtained, which effectively regulates the electromagnetic properties and achieves coupling of dielectric–magnetic attenuation through the component synergistic effect [24]. Owing to their excellent ferromagnetic properties, high Curie temperature, and strong magnetic loss capacity in the GHz band, cobalt nickel alloys (CoNi) have received widespread attention [25]. Recently, various MOF-derived CoNi@C composites with ingenious component arrangements and versatile microstructures have been developed for efficient EMW absorption materials [26–29]. For example, Yu *et al.* [29] prepared cubic hollow CoNi@C composites in which CoNi nanoparticles were distributed in a porous carbon matrix. Liu *et al.* [30] synthesized CoNi@C composites with a porous structure via the pyrolysis of bimetallic CoNi MOFs. Combining optimized impedance matching and enhanced attenuation capacity, the minimum reflection loss (RL_{min}) reaches −74.7 dB at 1.8 mm. Similarly, Xie *et al.* [31] fabricated a series of irregular rod-like MOF-derived CoNi@C composites. The results demonstrate that when the Co/Ni atomic ratio is 1, CoNi@C displays a maximum effective absorption bandwidth (EAB) of 4.77 GHz at 1.5 mm. Although controllable EAB and RL can be achieved, most composites suffer from magnetic property deterioration and interface area reduction owing to the agglomeration of CoNi nanoparticles, constraining the optimization of EMW absorption performance [32]. The latest research indicates that the construction of a built-in electric field (BIEF) within composites has emerged as a sophisticated and effective strategy for further enhancing the EMW absorption performance [33]. The BIEF can be actively engineered through rational compositional design and interfacial control, typically achieved by creating heterointerfaces between components with distinct work functions [34]. However, few reports on BIEF-based heterointerface engineering for efficient EMW absorption of MOF-derived Co_xNi_y@C composites are available. The effects of the Co/Ni atomic ratio and interface structure on the BIEF effect and EMW loss mechanisms are still unclear. Therefore, the fabrication of MOF-derived Co_xNi_y@C composites with strong BIEF effects and the determination of the corresponding role of the Co/Ni atomic ratio on the EMW absorption performance are highly desirable yet challenging.

Typically, the plane structure (uniform coating or panel) of EMW absorbers is difficult to apply in multiband compatible scenarios, which are restricted by the inherent electromagnetic parameters of the material [35–37]. Metamaterials can overcome this dilemma by combining EMW absorbers with artificially designed periodic unit structures (e.g., open resonance rings, fractal geometries, or metastructures) to achieve broadband EMW absorption at a certain thickness [38–40]. Wang *et al.* [41] fabricated a vanadium nitride@hierarchical porous carbon/cobalt@carbon nanotube (VN@HPC/Co@CNT) composite as an EMW absorber. After that, a metamaterial comprising VN@HPC/Co@CNT was designed and achieved a wide EAB of 12.55 GHz at a thickness of 2.77 mm. Zhang *et al.* [23] first synthesized a series of carbon-coated iron-based composites and systematically investigated their electromagnetic response characteristics. A symmetric gradient honeycomb structure (SGHS) coupled with a preferred carbon-coated iron-based composite was then simulated to further extend the EAB. The optimized SGHS achieves an EAB of 14.6 GHz and an RL_{min} of −59 dB with a total thickness of 30 mm. Thus, the multiscale structure design of the absorber can achieve broadband absorption at a certain thickness. However, current research rarely focuses on the cross-scale structural engineering of MOF-derived CoNi@C composites. Therefore, conducting an in-depth investigation into the EMW absorption performance and mechanism of a metamaterial composed of MOF-derived CoNi@C composites is essential.

Herein, a cross-scale structural design of a MOF-derived Co_xNi_y composite metamaterial with broadband EMW absorption was successfully achieved. First, bimetallic CoNi nitrilotriacetic acid chelate (CoNi–NTAC) precursors with various aspect ratios were synthesized by regulating the Co/Ni atomic ratio, followed by *in situ* pyrolysis to obtain Co_xNi_y@C composites. The work function difference between Co_xNi_y and C creates BIEFs and enriches heterogeneous interfaces, enhancing the dielectric loss capacity. Additionally, Co_xNi_y nanoparticles confined within the carbon matrix exhibit strong magnetic resonance. Thus, Co_2Ni@C has excellent EMW absorption performance, with an EAB covering 4.9 GHz at 1.75 mm. The metamaterial was subsequently designed to further broaden the EMW absorption performance of Co_2Ni@C. The simulated EAB of the gradient honeycomb structure (GHCS) metamaterial reached 38 GHz (2–40 GHz) at a total thickness of 15 mm. Moreover, the broadband absorption mechanism of the proposed GHCS was investigated via CST Microwave Studio. This study provides valuable insights into the electromagnetic loss mechanisms of MOF-derived Co_xNi_y@C composites and achieves broadband EMW absorption through innovative cross-scale structural design.

2 Experimental

2.1 Raw materials

Cobalt chloride hexahydrate ($CoCl_2·6H_2O$), nickel chloride hexahydrate ($NiCl_2·6H_2O$), isopropyl alcohol, nitrilotriacetic acid, and anhydrous ethanol were purchased from Sinopharm Chemical Reagents Co., Ltd. All the chemicals and reagents were of analytical grade and were used directly without further purification.

2.2 Fabrication of MOF-derived Co_xNi_y@C nanorods

MOF-derived Co_xNi_y@C nanorods were fabricated via solvothermal methods and subsequent pyrolysis. Initially, 30 mL of deionized water and 30 mL of isopropyl alcohol were stirred magnetically for 2 h with 0.8 g of $CoCl_2·6H_2O$, 0.8 g of $NiCl_2·6H_2O$, and 0.6 g of nitrilotriacetic acid. The solution was subsequently transferred into a 100 mL Teflon-lined stainless-steel autoclave and kept at 160 °C for a duration of 6 h. The precipitate was separated by centrifugation and dried in a vacuum oven at 60 °C overnight. Finally, the CoNi@C nanorods were obtained by pyrolysis at a rate of 2 °C/min under an argon atmosphere. The amounts of $CoCl_2·6H_2O$ used were 0.8, 1.6, and 2.4 g, and the resulting samples were denoted as CN1, CN2, and CN3, respectively.

2.3 Characterizations

The morphology and microstructure of the composites were characterized via a field emission scanning electron microscope (FESEM; Sigma 300, ZEISS) and a transmission electron microscope (TEM; Themis Z, FEI). The crystal structure, phase composition, and elemental valence of the composites were analyzed via an X-ray diffractometer (XRD; D8-Advance, Bruker) with Cu-Kα radiation and an X-ray photoelectron spectroscope (XPS; Thermo Fisher Scientific). The graphitization degree of the carbon in the composites was recorded via a Raman spectroscope (Renishaw in Via plus, Renishaw). To determine the proper

pyrolysis temperature, the thermogravimetric (TG) curves of the precursors were investigated via an SDTQ600 analyzer (TA Instruments). The magnetic properties of the composites were obtained via a vibrating sample magnetometer (7404, Lakeshore). The electromagnetic parameters in the 1–18 GHz range were tested via the coaxial method by mixing the composites (20 wt%) with paraffin wax.

2.4 CST simulation

The EMW absorption performance of the metamaterial was simulated via CST Studio Suite software. First, a geometric model of the metamaterial was constructed, incorporating an aluminum plate as a metallic backplane at the bottom. The electromagnetic parameters of the unit cell were assigned according to the tested complex permittivity and permeability of the MOF-derived CoNi@C composites within 2–18 GHz. According to the Debye equation, the electromagnetic parameters were extrapolated from 2–18 GHz to cover 2–40 GHz, with the fitting error constrained to within 1%. Periodic boundary conditions were applied along the *X* and *Y* directions, whereas an open (free space) boundary was set in the *Z* direction. Two waveguide ports were employed to excite the unit cell with a transverse electromagnetic plane wave incident normally. The RL of the metamaterial was simulated via the frequency domain solver, which also enabled the analysis of electromagnetic characteristics (such as the electric field distribution, magnetic field distribution, and power loss density) at the absorption peak frequency.

The DFT calculations are presented in the Electronic Supplementary Material (ESM).

3 Results and discussion

3.1 Fabrication and characterization of MOF-derived Co_xNi_y@C nanorods

The procedure for the preparation of MOF-derived Co_xNi_y@C nanorods is illustrated in Fig. 1(a). A series of CoNi-MOFs were fabricated via the solvothermal method using nitrilotriacetic acid as the organic ligand, and Co^{2+} and Ni^{2+} served as the main metal species. To analyze the mass changes and chemical reactions of the precursors, TG curves were measured under an argon atmosphere from room temperature to 900 °C. The whole pyrolysis reaction is organized into three stages (Fig. S1 in the ESM). In stage I, a slight weight decrease of 3% before 209 °C was

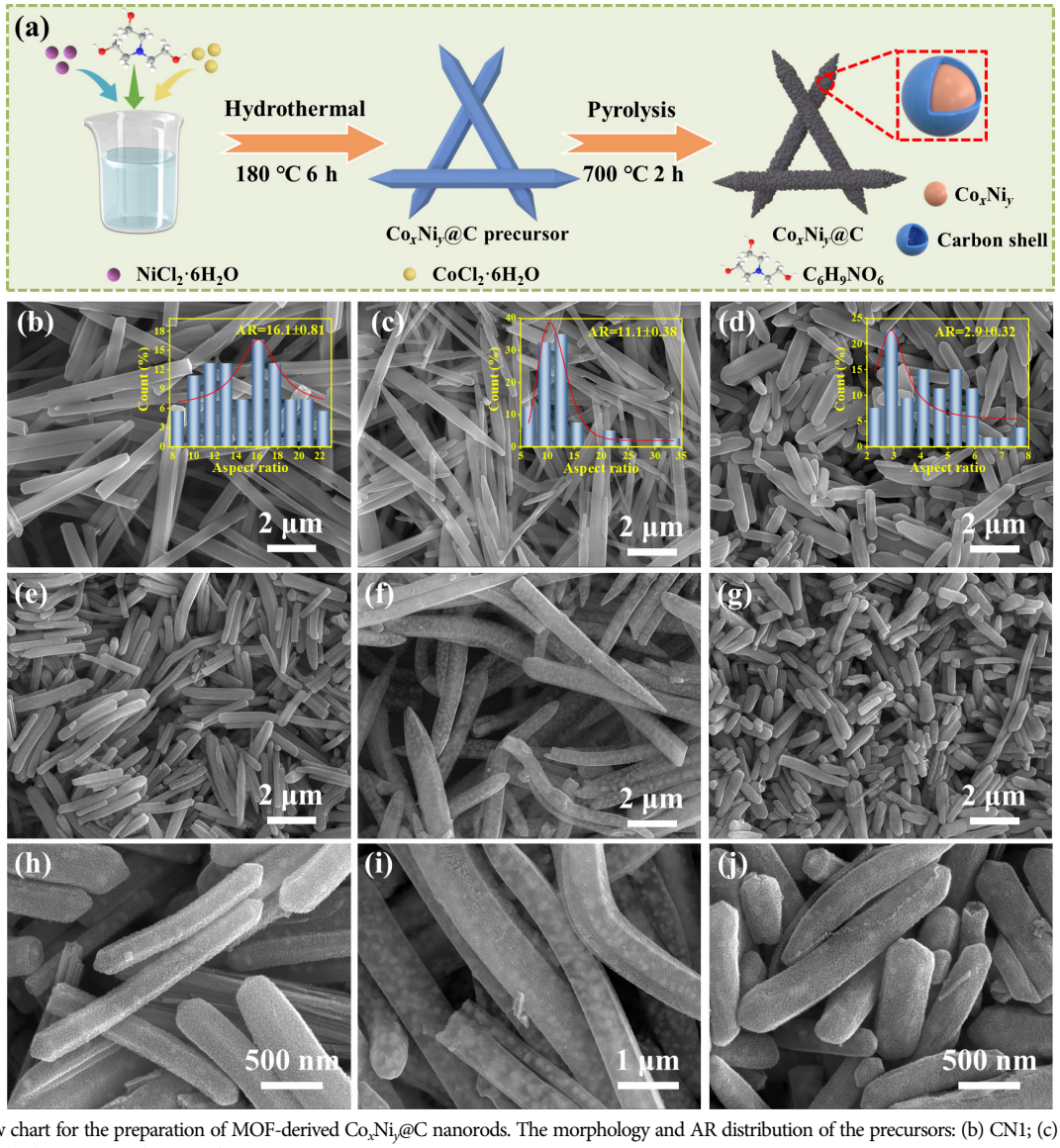

Fig. 1 (a) Flow chart for the preparation of MOF-derived Co_xNi_y@C nanorods. The morphology and AR distribution of the precursors: (b) CN1; (c) CN2; (d) CN3. SEM images of the derivatives: (e, h) CN1; (f, i) CN2; (g, j) CN3.

observed was attributed to the volatilization of the crystalline water in the composites. The weight loss of 23.5% in stage II corresponds to the decomposition of organic ligands. The significant weight decrease of 41.2% in stage III is attributed to the carbonization of organic matter to form pyrolytic carbon while reducing Co^{2+} and Ni^{2+} to CoNi nanoparticles. The total mass maintenance of the precursors is approximately 20%. The TG results indicate that the pyrolysis process can be completed when the temperature is above 420 °C. Thus, the Co_xNi_y@C precursors were pyrolyzed at 700 °C, and the corresponding phase composition and microstructure were characterized.

Anisotropic growth leads to Co_xNi_y@C precursors with a hexagonal rod shape (Figs. 1(b)–1(d)). Interestingly, the content of Co^{2+} strongly affects the morphology of the Co_xNi_y@C precursor. The larger the Co^{2+} amount is, the shorter the length of the nanorod. The AR of the precursors decreased from 16.1 to 2.9. Generally, the large AR of one-dimensional nanorod-like structures facilitates the transportation and hopping of electrons and the construction of three-dimensional conductive networks, increasing the conductive loss capacity. After high-temperature pyrolysis, the derivatives decreased in size and bent owing to the decomposition of organic ligands but still preserved the basic structure of the precursors. In addition, the surface of the composites became rough, and many nanoparticles with variable sizes were evenly distributed. Figures S2–S4 in the ESM display the element mapping and corresponding atomic percentages of the composites. The C, Co, and Ni elements are uniformly distributed, and the atomic percentages of Co/Ni are 1.04, 1.9, and 2.81, respectively. The energy dispersive spectroscopy (EDS) results demonstrate that the precursors have successfully transformed into CoNi@C, Co_2Ni@C, and Co_3Ni@C, which is in accordance with the expected experimental design.

The detailed microstructure of the CN2 precursor is shown in Fig. S5 in the ESM. The TEM results demonstrate that the profile of the precursor is a hexagonal nanorod, which is similar to the SEM images (Fig. S5(a) in the ESM). The high-resolution TEM (HRTEM) image shows that the precursor is composed of a matrix and dispersed nanoparticles (Fig. S5(c) in the ESM). In the solvothermal process, nitrilotriacetic acid acts as a linker to tightly anchor Co^{2+} and Ni^{2+} via chelation; therefore, a distinct hierarchical structure is formed. After high-temperature calcination, the nanoparticles with various diameters and dense structures were encapsulated in the carbon matrix (Figs. 2(a), 2(e), and 2(i) in the ESM). Owing to Ostwald ripening, the emergence of large particles comes at the expense of small particles. Figure 2(c) shows that the lattice stripe of the nanoparticle is 0.12 nm, corresponding to the (220) plane of CoNi. In addition, distinct continuous graphitic carbon (GC) layers are homogeneously wrapped around the CoNi. The measured lattice stripe of the GC is 0.34 nm, belonging to the (002) plane. The emergence of the GC is mainly attributed to the catalytic effect of the CoNi alloy at high temperatures, whereas the region away from the CoNi remains amorphous carbon. Bright diffraction circles in selected area electron diffraction (SAED) correlate to the (111), (200), and (220) planes of CoNi, indicating a polycrystalline structure. The spatial distributions of C, Co, and Ni further demonstrate that the CoNi nanoparticles are uniformly distributed in the carbon matrix. In the HRTEM images of CN2 (Fig. 2(h)), the clear lattice fringes with interlayer spacings of 0.12 and 0.21 nm correspond to the (220) and (111) crystal planes of CoNi. Notably, there are

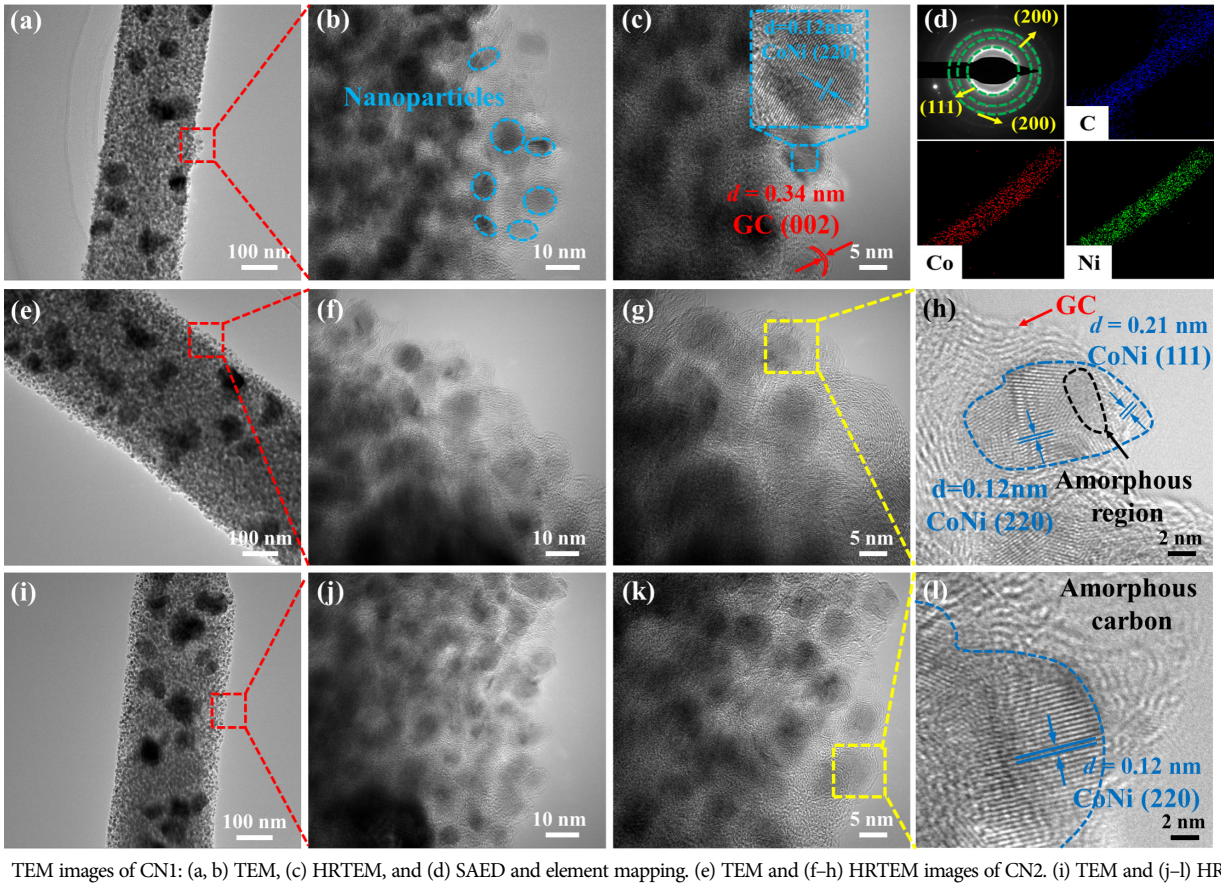

Fig. 2 TEM images of CN1: (a, b) TEM, (c) HRTEM, and (d) SAED and element mapping. (e) TEM and (f–h) HRTEM images of CN2. (i) TEM and (j–l) HRTEM images of CN3.

some distortions and lattice defects in the CoNi nanoparticles, which act as dipoles to trigger dipole polarization at high frequencies. The microstructure of CN3 is similar to that of CN1 and CN2, consisting of CoNi, GC, and amorphous carbon.

The XRD results demonstrate that the Co_xNi_y@C precursors are composed of CoOOH and NiOOH. In addition, the intensity of the diffraction peaks decreases with increasing Co^{2+} content (Fig. S6 in the ESM). The composition and phase information of the derivatives after high-temperature pyrolysis are shown in Fig. 3(a). Three pronounced diffraction peaks, located at 44.4°, 51.8°, and 76.2°, correspond to the (111), (200), and (220) crystal planes of CoNi, respectively. Notably, the intensity of the diffraction peaks varies with the concentration of Co^{2+}, revealing that the crystallinity of CoNi can be adjusted by the Co content. Figure 3(b) displays the Raman curves of the carbon matrix in the composites. All the samples exhibited two peaks: the peaks at 1350 and 1580 cm^{-1} represented the D band and G band, respectively [42,43]. The intensity ratio of the D band to the G band (I_D/I_G) was used to characterize the level of graphitization of the carbon matrix [44]. The I_D/I_G values for CN1, CN2, and CN3 are 0.98, 0.79, and 0.86, respectively. CN2 has the lowest value of I_D/I_G, demonstrating that more graphite carbon is generated under CoNi catalysis, which is beneficial for increasing the conductivity. XPS was conducted to analyze the element valence states of the three samples. As shown in Fig. 3(c), all the samples contained C, O, Co, and Ni. The C 1 s peak can be separated into two peaks, and the peaks located at 284.8 and 286.2 eV represent C–C and C–O, respectively (Fig. 3(d)). The Co element mainly consisted of "0" and "+2" valence states, demonstrating that the surface mainly contains Co and CoO. The presence of CoO is due to slight oxidation (Fig. 3(e)). For Ni 2p, the valence states are similar to those of Co 2p, and the spectra can be divided into eight peaks, namely, Ni $2p_{3/2}$ (853.04 eV), Ni $2p_{1/2}$ (870.12 eV), Ni^{2+} $2p_{3/2}$ (854.48 eV), Ni^{2+} $2p_{1/2}$ (872.64 eV), and two satellite peaks (858.9 and 876.1 eV).

3.2 Tunable EMW absorption performance and attenuation mechanism of composites

RL and EAB are two critical factors commonly used to assess a material's EMW absorption performance. The values of RL and EAB were calculated via Eqs. (1) and (2):

$$Z_{in} = Z_0\sqrt{\frac{\varepsilon}{\mu}}\tanh\left(\frac{j2\pi fd\sqrt{\varepsilon\mu}}{c}\right) \quad (1)$$

$$RL = 20\log\left|\frac{Z_{in}-Z_0}{Z_{in}+Z_0}\right| \quad (2)$$

where ε, μ, f, d, c, Z_{in}, and Z_0 are the complex permittivity, complex permeability, EMW frequency, thickness of the material, light speed, input impedance, and free space impedance, respectively. Figures 4(a)–4(c) show two-dimensional (2D) images of the RL versus thickness and frequency. The Co/Ni atomic ratio clearly has a considerable influence on the EMW absorption performance. CN1 has difficulty realizing effective absorption when the thickness is less than 3 mm and exhibits dual-band absorption at low and high frequencies for thicknesses greater than 4.1 mm (Fig. 4(a)). In Fig. 4(b), CN2 possesses superior EMW absorption performance, with the EAB reaching 4.9 GHz (13.1–18 GHz) at 1.75 mm. As the Co/Ni atomic ratio further increases, CN3 has the weakest EMW absorption performance: the EAB and RL_{min} decrease to 1.9 GHz and −11.2 dB, respectively (Fig. 4(c)). In addition, the frequency corresponding to the absorption peak progressively decreases with increasing thickness, following the quarter-wavelength interference cancellation theory (Figs. 4(d)–4(f)). According to the optimum EAB and RL_{min} of the composites illustrated in Fig. 4(g), the EAB and RL_{min} of CN2 are 4.9 GHz and −46.9 dB, respectively, indicating the best EMW absorption performance. Comparison of the EMW absorption performance of fabricated CN2 with materials recently reported in the literature (Fig. 4(h) and Table S2 in the ESM). Obviously, the

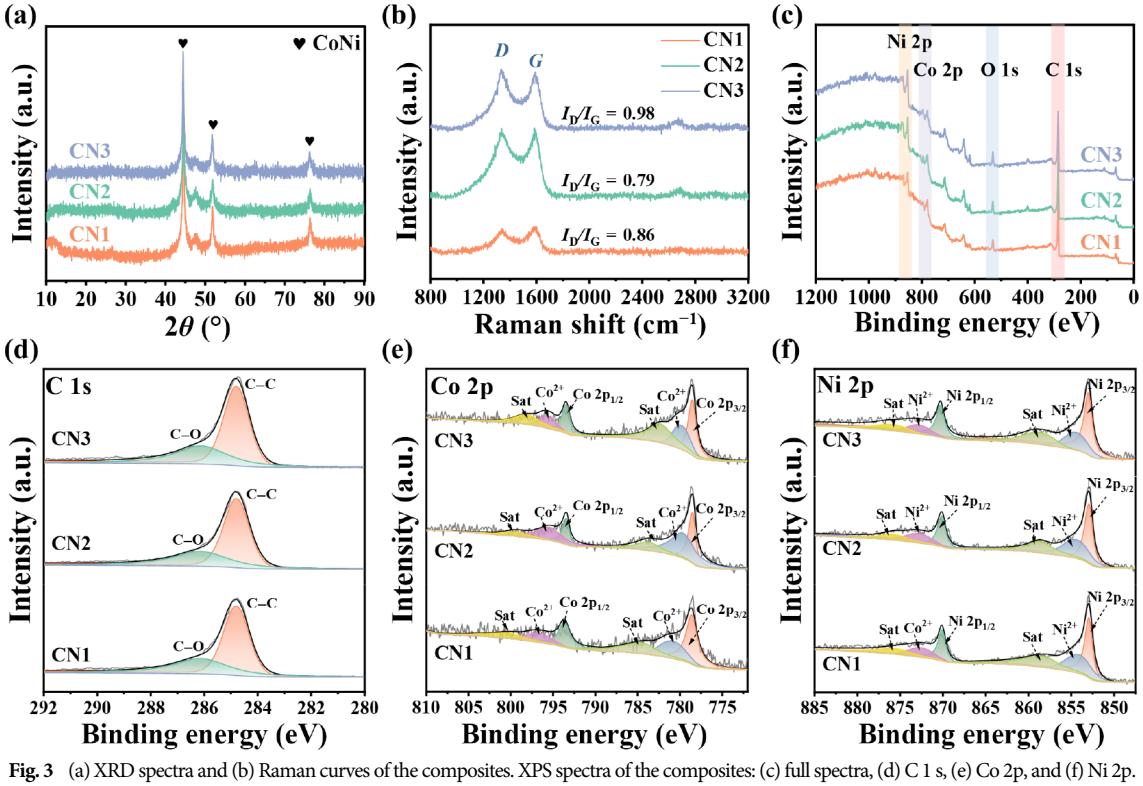

Fig. 3 (a) XRD spectra and (b) Raman curves of the composites. XPS spectra of the composites: (c) full spectra, (d) C 1 s, (e) Co 2p, and (f) Ni 2p.

unique hierarchical nanorod-structured and ingenious component design endows CN2 with distinguished absorption properties: the optimum EAB and the thinnest matching thickness at the lowest fill level surpass the majority of reported materials [45–54]. A radar cross-section (RCS) simulation of the composites under the strongest absorption frequency was conducted to further evaluate the potential for practical application. As shown in Figs. 4(i) and 4(j), compared with that of the PEC substrate, the scattering signal intensity of the PEC substrate covered with CN2 is significantly lower. In addition, the corresponding 1D curves indicate that CN2 exhibits exceptional RCS reduction performance across all angles. Furthermore, the RCS reduction effect at 0°, 30°, 60°, and 90° was calculated by subtracting the RCS value of the PEC. The fabricated composites exhibit maximum RCS reduction at a direction angle of 0°, and the corresponding reduction values of the three composites are 7.9, 15.8, and 4.6 dB·m^2. Thus, the RCS calculation results indicate that the CN2 composite can effectively suppress the scattering of EMW, demonstrating that CN2 is a promising candidate EMW absorption material.

By modulating the atomic ratio of Co/Ni, the MOF-derived hexagonal nanorod-like Co_2Ni@C composite with a moderate AR exhibited outstanding EMW dissipation ability and broadband absorption performance. Thus, the related dielectric and magnetic properties were investigated to further analyze the corresponding EMW absorption mechanism.

(i) Enhanced polarization and conductive losses by tuning the Co/Ni atomic ratio. The dielectric constant of the composites was measured to illustrate the dielectric loss mechanism, as shown in Figs. 5(a) and 5(b). The ε' decreases approximately with increasing frequency, exhibiting frequency dispersion characteristics (Fig. 5(a)), whereas ε'' first decreases and subsequently increases with increasing frequency (Fig. 5(b)). Moreover, some resonance peaks can be observed in CN2, which demonstrates the existence

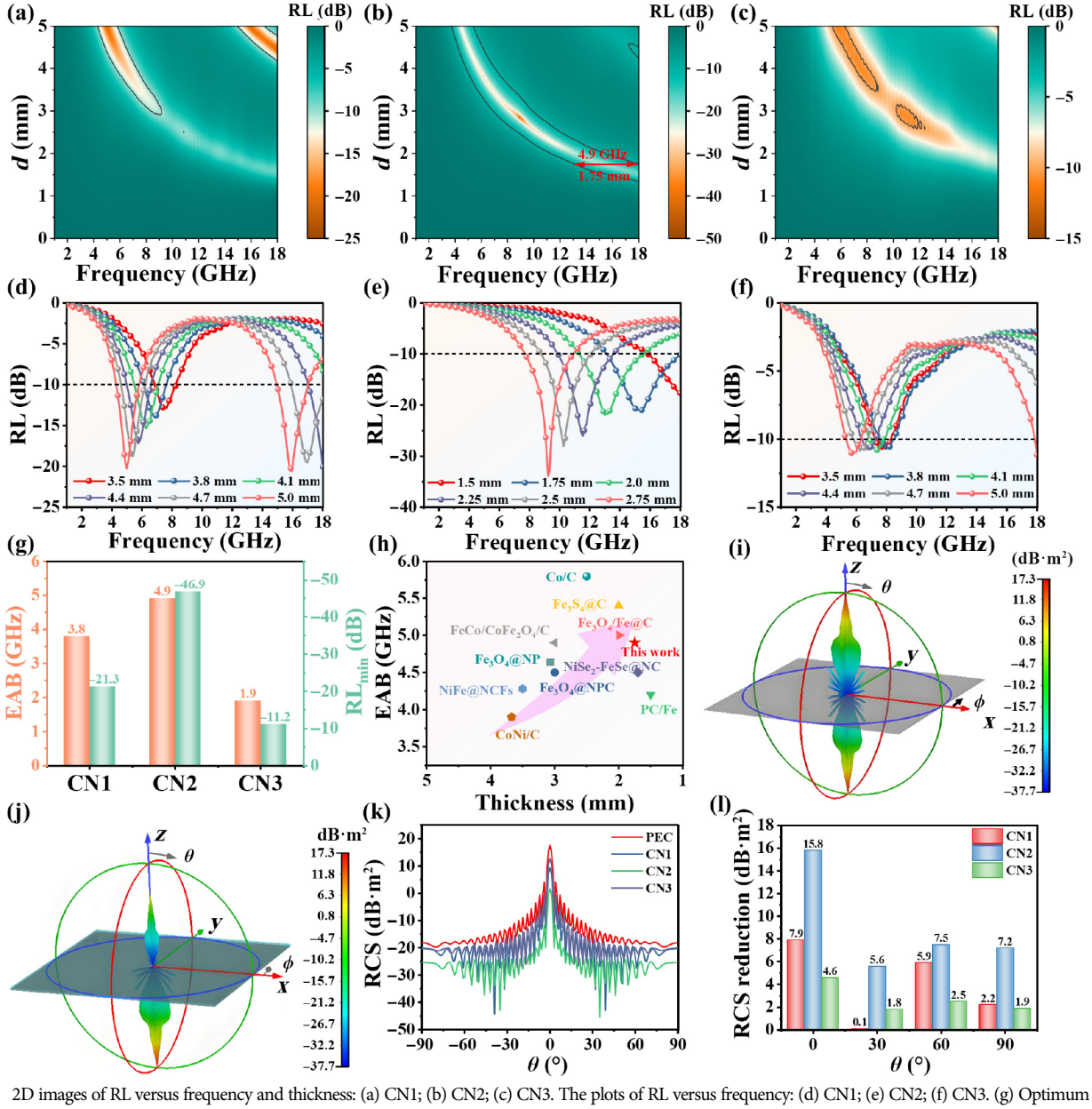

Fig. 4 2D images of RL versus frequency and thickness: (a) CN1; (b) CN2; (c) CN3. The plots of RL versus frequency: (d) CN1; (e) CN2; (f) CN3. (g) Optimum EAB and RL_{min} of the composites. (h) Comparison of the EMW absorption performances of CN2 and the reported materials. 3D RCS plots of the (i) PEC substrate and (j) PEC substrate covered with CN2. (k) Simulated RCS values of PECs and PECs covered with composites. (l) RCS reduction values.

of strong EMW attenuation behavior. The resonant peaks can be attributed to various polarization relaxations within CN2, including dipole polarization generated by defects in the carbon matrix and interfacial polarization arising from high-density nanosized heterogeneous interfaces (Co_2Ni/graphitic carbon, Co_2Ni/amorphous carbon, and graphitic carbon/amorphous carbon interfaces). The tangent of dielectric loss ($\tan\delta_\varepsilon = \varepsilon''/\varepsilon'$) is calculated to evaluate the dielectric loss capability, and the order of $\tan\delta_\varepsilon$ is CN2 > CN1 > CN3 (Fig. 5(c)). The work function, density charge density, and difference of states (DOS) at the Co_xNi_y/C heterogeneous interfaces were investigated via DFT calculations to further analyze the dielectric loss mechanism of the composites. Figure S7 in the ESM displays the modeling of the Co_xNi_y/C heterogeneous interfaces via DFT. Typically, the value of work function (W) equals the difference between the vacuum energy level (E_{vac}) and the Fermi energy level (E_{fermi}). Thus, the calculated work functions of C, CoNi, Co_2Ni, and Co_3Ni are 4.6639, 4.5847, 4.8303, and 4.5847 eV, respectively (Figs. 5(d)–5(f), Fig. S8 in the ESM). The work functions of Co_2Ni and Co_3Ni are greater than that of C, which indicates that Co_2Ni and Co_3Ni possess higher Fermi energy levels. The difference in work function between C and Co_2Ni and Co_3Ni drives the directional migration of electrons. Valence band bending occurs when C contacts Co_2Ni and Co_3Ni, and electrons continuously migrate from C to Co_2Ni and Co_3Ni, leading to the formation of BIEFs [55]. The absolute values of the work function differences at the Co_xNi_y/C interfaces are 0.0792, 0.1664, and 0.0399 eV, demonstrating the fastest charge migration and the stronger BIEF effect at the Co_2Ni/C interface. Figures 5(g)–5(i) display the calculated DOS of the Co_xNi_y/C interfaces. A large difference in electronegativity increases electron cloud displacement, enhancing dipole polarization. The large electronegativity between Co_2Ni and C results in the strongest dipole polarization at the Co_2Ni/C interface. In addition, the charge is redistributed at the Co_xNi_y/C interface, with electron accumulation at Co_xNi_y and electron depletion at C (Figs. 5(g)–5(i)). The yellow color represents

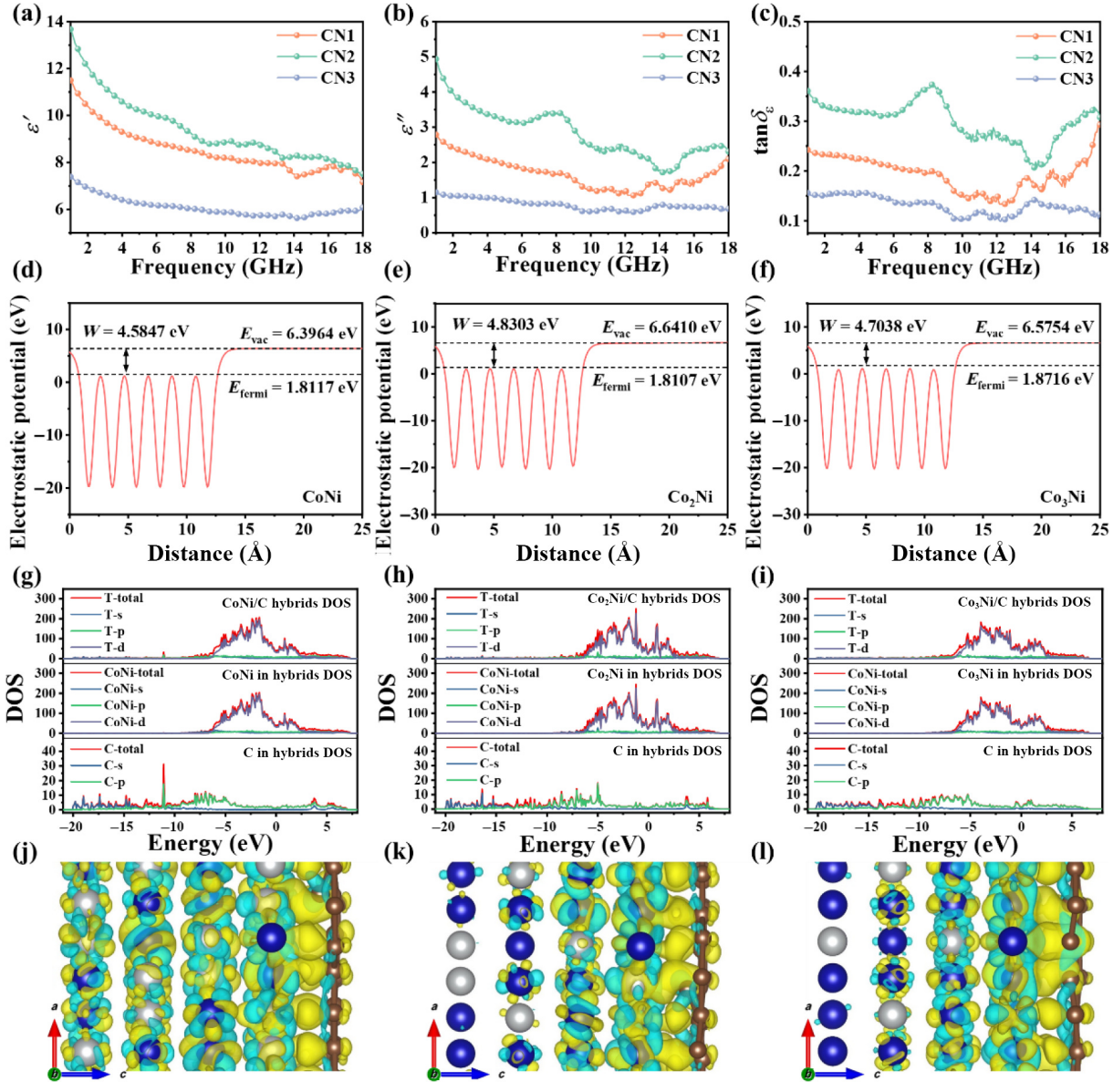

Fig. 5 Dielectric constant and dielectric loss tangent of the composites: (a) ε', (b) ε'', (c) $\tan\delta_\varepsilon$. The calculated work functions of (d) CoNi, (e) Co_2Ni, and (f) Co_3Ni. (g–i) DOS of the interfaces of three composites obtained from DFT calculations. The charge density distributions of the Co_xNi_y/C heterointerfaces: (j) CN1, (k) CN2, and (l) CN3.

electron enrichment, whereas the turquoise color represents electron deficiency. Significant charge enrichment at the Co_2Ni/C interface can be observed, while the Co_3Ni/C interface has the lowest charge density (Figs. 5(k) and 5(l)) [56]. Overall, a strong BIEF facilitates electron accumulation and migration, endowing CN2 with enhanced polarization and conductive loss capacity.

Furthermore, the dielectric loss mechanism of the composites is analyzed via the Debye equations, as shown in Eqs. (3)–(5):

$$\varepsilon' = \varepsilon_\infty + \frac{\varepsilon_s - \varepsilon_\infty}{1 + \tau^2\omega^2} \tag{3}$$

$$\varepsilon'' = \varepsilon_p'' + \varepsilon_s'' = \frac{\varepsilon_s - \varepsilon_\infty}{1 + \tau^2\omega^2} + \frac{\sigma}{\omega\varepsilon_0} \tag{4}$$

$$\left(\varepsilon' - \frac{\varepsilon_s - \varepsilon_\infty}{2}\right)^2 + \varepsilon''^2 = \left(\frac{\varepsilon_s - \varepsilon_\infty}{2}\right)^2 \tag{5}$$

where ε_s, ε_∞, σ, ω, and τ are the static permittivity, permittivity at infinite frequency, conductivity, angular frequency, and relaxation time, respectively. According to Eq. (4), ε'' consists of polarization loss (ε_p'') and conductive loss (ε_c''). Polarization loss can be divided into interface polarization and dipole polarization. When the polarization loss originates solely from dipole polarization, the curves of ε' and ε'' are normal semicircles, called Cole–Cole semicircles, where each semicircle represents one type of polarization relaxation. Several distorted semicircles can be observed in CN1 and CN2, demonstrating the existence of multiple polarization relaxations at high frequencies (Figs. 6(a) and 6(b)). For CN3, there is a vague arc in Fig. 6(c) because of the inferior dielectric loss capacity. In addition, a straight line appears in Figs. 6(a) and 6(b), which represents the conductive loss, implying that the conductive loss is the primary dissipation form in the low-frequency range. Eq. (4) is simplified to facilitate further discussion of ε_p'' and ε_c''. If ε_p'' is neglected, ε'' is linearly related to $1/f$, and the slope is $\sigma/(2\pi\varepsilon_0)$ [57]. As shown in Fig. S6(a) in the ESM, the relationship between ε'' and $1/f$ remains a straight line when $0.2 < 1/f < 1$, and the slope corresponds to the conductivity. The order of conductivity inferred from the magnitude of the slope is $\sigma_{CN2} > \sigma_{CN1} > \sigma_{CN3}$. In addition, the intercept of the straight lines is constant, suggesting a weak polarization loss in the 1–4.8 GHz range. However, ε'' vs. $1/f$ cannot be linearly maintained in the 4.8–18 GHz range, indicating that the contribution of polarization loss to dielectric loss is not negligible. When solely considering the contribution of polarization loss, the equation can be converted to $\varepsilon''/f = 2\pi\tau\varepsilon' - A$, where ε''/f has a linear relationship with ε' [58]. Figures 6(e)–6(g) show that the slopes of the linear segments of the ε''/f–ε' plots for CN1, CN2, and CN3 are 1.46, 1.58, and 1.32, respectively. Thus, the calculated relaxation time (τ) and frequency (f) are 0.23×10^{-11} s and 4.3 GHz, 0.27×10^{-11} s and 3.9 GHz, and 0.21×10^{-11} s and 4.7 GHz, respectively (Fig. S9(b) in the ESM). The polarization frequencies of the composites fall within the range of 1–5 GHz, indicating that this frequency band exhibits slight polarization loss. When the electric field frequency ranges from 1–5 GHz, the dipoles and heterointerfaces within the composites can follow the variation in the EMW without any hysteresis effect. As the frequency increases, the moment of the dipoles fails to keep pace with the variation in the EMW, exhibiting strong polarization loss, resulting in a nonlinear region in Fig. S9(a) in the ESM. Consequently, tuning the Co/Ni atomic ratio of composites can modulate the polarization loss and conductive loss, realizing enhanced dielectric dissipation.

(ii) Superior magnetic loss can be achieved by constructing multiple magnetic coupling networks. The magnetic loss capacity of composites is closely related to their complex permeability. In Fig. 7(a), μ' of the composites decreases with increasing frequency, which is in accordance with Snoek's limit. Notably, μ'' is closely associated with the Co/Ni atomic ratio and gradually increases with increasing Co/Ni ratio. Figure 7(b) displays two resonance peaks: a natural resonance at 5 GHz and an exchange resonance at 13 GHz. The negative values of CN1 in μ'' may be attributed to the release of magnetic energy from the conductive network due to the induced alternating magnetic field generated by the motion of free electrons in an alternating electric field. The calculated tan δ_μ values are shown in Fig. 7(c), where CN-2 and CN-3 exhibit excellent magnetic loss capacities. CN-3 has the strongest natural resonance at low and middle frequencies, whereas both CN-2 and CN-3 have strong exchange resonances at high frequencies. The saturation magnetization (M_s) and coercivity (H_c) in the hysteresis loops reflect the intrinsic magnetic properties of the composites (Fig. 7(d)). The M_s increased from 49.5 emu/g to 111.7 emu/g with increasing Co^{2+} content. This is

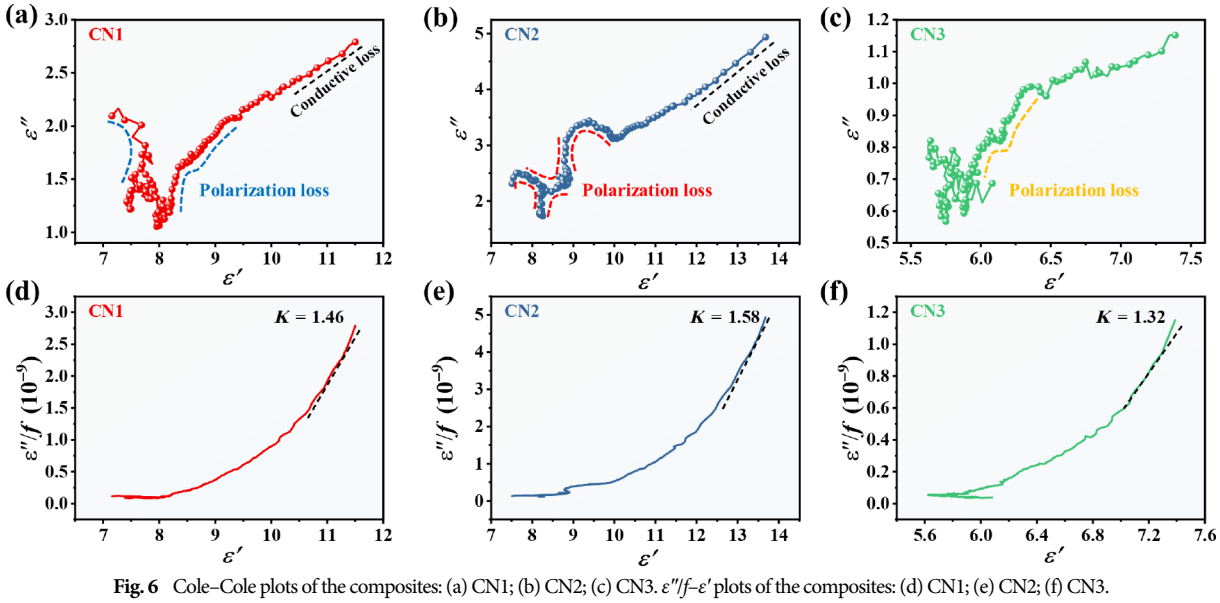

Fig. 6 Cole–Cole plots of the composites: (a) CN1; (b) CN2; (c) CN3. ε''/f–ε' plots of the composites: (d) CN1; (e) CN2; (f) CN3.

because the atomic magnetic moment of Co is larger than that of Ni; therefore, M_s increases linearly when the content of Co atoms gradually increases. The variation tendency of H_c is consistent with that of M_s, increasing from 211.2 to 352.5 Oe. The relationship between M_s, H_c, and μ_i is shown in Eq. (6) [59]:

$$\mu_i = \frac{M_s^2}{akH_cM_s + b\lambda\xi} \quad (6)$$

where a and b are material constants, k is the proportionality coefficient, λ is the magnetostrictive coefficient, and ξ is the internal strain. According to Eq. (6), the higher the M_s is, the stronger the magnetic loss capability. Moreover, the eddy current loss ($C_0 = \mu''(\mu')^{-2}(f)^{-1}$) was calculated to analyze the magnetic loss mechanism [60]. The values of C_0 vary throughout the 1–18 GHz; thus, the contribution of eddy current loss can be excluded (Fig. 7(f)). Notably, the peak that appears at approximately 12 GHz is attributed to the exchange resonance. On the basis of the aforementioned results, the magnetic loss of composites is caused mainly by resonance loss.

(iii) Excellent impedance matching and strong attenuation characteristics. In general, superior impedance matching and strong attenuation are two prerequisites for broadband absorption. In Figs. 8(a)–8(c), the attenuation constant (α) values of the composites increase with increasing frequency, implying strong EMW dissipation at high frequencies. CN2 has the strongest EMW dissipation ability in the whole test frequency band. The normalized impedance matching values ($|Z_{in}|$) of the composites with various thicknesses and frequencies are calculated via Eq. (1). The range of $0.8 \le |Z_{in}| \le 1.2$ is used to evaluate the impedance matching, as shown in Figs. 8(d)–8(f) [61,62]. Typically, excellent impedance matching is indicated by large areas of $0.8 \le |Z_{in}| \le 1.2$. The calculated area ratios of $0.8 \le |Z_{in}| \le 1.2$ are 8.3%, 12%, and 8.4%, respectively. CN2 has the largest area, demonstrating its superior impedance-matching characteristics. The superior impedance matching of CN2 is attributed to the enhanced dielectric and magnetic loss capacity, which allows more EMW to penetrate into the absorber.

On the basis of the above analysis, the superior EMW absorption performance of Co_2Ni@C primarily stems from the synergistic effect of well-balanced electromagnetic properties and rationally designed heterostructures. The potential EMW attenuation mechanisms of CN2 are illustrated in Fig. 9. (i) Enhanced polarization loss. The enrichment of nanosized CoNi particles within the carbon matrix creates abundant heterogeneous interfaces and Schottky junctions. Electrons migrate from the low-work-function carbon matrix to Co_2Ni with a high work function, establishing a BIEF at the Co_2Ni/C interface. The constructed BIEF can restrict electron transfer and prolong the electron relaxation time, thereby enhancing the polarization loss effect. Moreover, defects (lattice distortion and atom defects) in graphitic carbon and CoNi can act as dipole centers and induce dipole polarization. (ii) Increased conductive loss. The joint contribution of the d-orbital of Co_2Ni increases the DOS, enhancing the conductive loss capacity. The emergence of graphite carbon layers around the Co_2Ni nanoparticles increases the conductivity. Furthermore, the 1D hierarchical nanorod structure with a high AR establishes a conductive network, prolonging the propagation path of the EMW. (iii) Considerable magnetic loss. Uniformly dispersed CoNi nanoparticles contribute to strong magnetic resonance and afford sufficient magnetic loss, which improves the attenuation capability while reducing the matching thickness of absorbers. (iv) Optimized impedance matching. The hierarchical nanorod structure with a cooperative dielectric/magnetic loss capability endows composites with superior impedance matching.

3.3 Simulation results of the GHCS metamaterial

The variable EMW absorption performance of Co_xNi_y@C can be obtained at a certain thickness by regulating the Co/Ni atomic ratio. However, the single-band narrowband absorption of absorbers caused by inferior impedance matching at broadband limits practical engineering applications. Owing to its excellent attenuation capacity, CN2 is applied as a lossy component of the metamaterial. Compared with other metastructures, the honeycomb structure (HCS) displays significant advantages of being lightweight, having high strength, having a bionic design,

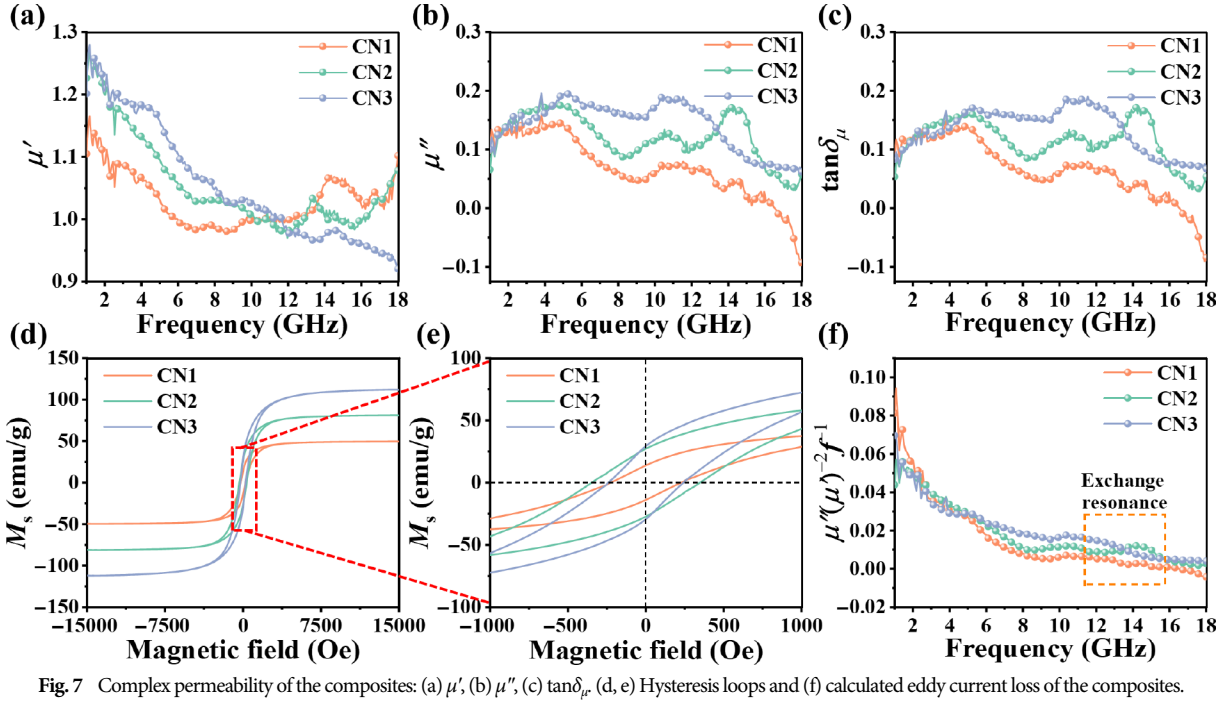

Fig. 7 Complex permeability of the composites: (a) μ', (b) μ'', (c) $\tan\delta_\mu$, (d, e) Hysteresis loops and (f) calculated eddy current loss of the composites.

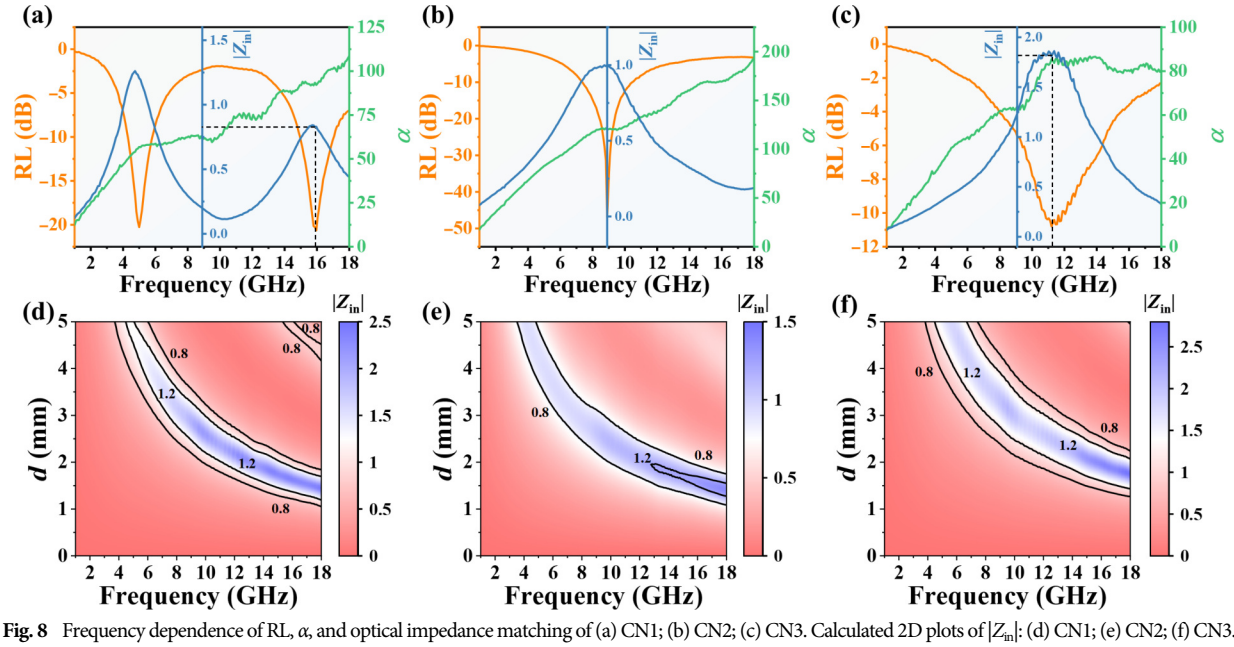

Fig. 8 Frequency dependence of RL, α, and optical impedance matching of (a) CN1; (b) CN2; (c) CN3. Calculated 2D plots of $|Z_{in}|$: (d) CN1; (e) CN2; (f) CN3.

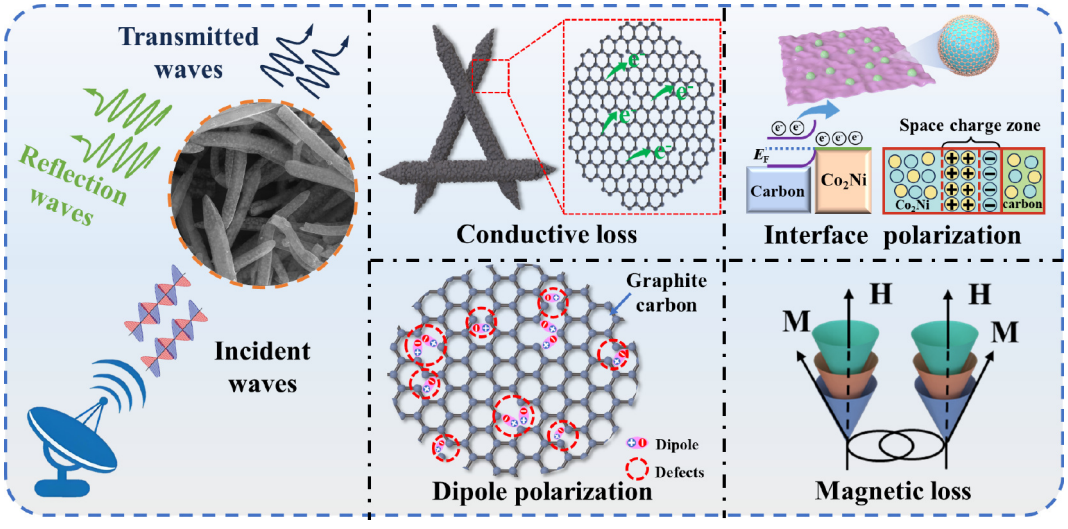

Fig. 9 Schematic diagram of the EMW attenuation mechanisms of CN2.

and having optimized impedance matching. Specifically, the diameter and wall thickness of the gradient honeycomb structure (GHCS) vary along the EMW incidence direction, creating a continuous transition of the equivalent permittivity and permeability, which effectively reduces the interfacial reflection of the incident EMW. Thus, the EMW absorption performance and corresponding attenuation mechanism of the GHCS metastructure coupled with CN2 were simulated. In addition, the flat structure (FS) and honeycomb structure (HCS) without a gradient structure at the same thickness were also calculated. The geometric parameters of the HCS and GHCS are optimized via CST Microwave Studio (Fig. 10(a)). Figure 10(b) displays the simulated RL of the FS, HCS, and GHCS with optimal parameters. Inadequate impedance matching results in inferior EMW absorption performance of the FS: the RL value of the FS is almost greater than −10 dB at 2–40 GHz. For HCSs, the EAB covers 2.6–4 and 8–30.3 GHz; however, the absorption intensity is significantly reduced in the C and Ka bands. Compared with the FS and HCSs, the GHCSs exhibit broadband and strong EMW absorption performance, the EAB reaches 38 GHz (2–40 GHz), and the RL_{min} is −50.7 dB at 26.3 GHz. In addition, the EMW absorption performance of the GHCSs under oblique incidence angles from 5° to 60° was calculated to broaden the application scenario. As shown in Fig. 10(c), the EMW absorption performance of the GHCSs remains stable within 5°–20° and slightly decreases with increasing incident angle. Notably, the EAB still remains at 31.5 GHz when the incident angle reaches 60°, indicating superior oblique incidence stabilization. The power loss distributions of the GHCSs at four absorption peak frequencies were simulated via CST to analyze the ultrabroadband absorption mechanism. At the lowest frequency (3 GHz), the power loss is distributed mainly in the inner wall and edges of the upper surface of the honeycomb structure, demonstrating that the GHCSs facilitate incident EMW propagation into the interior, effectively dissipating low-frequency EMW through multiple reflections and edge diffraction. At 14.2 GHz, the distribution of power loss is consistent with that at 3 GHz, whereas the absorption intensity gradually increases. For high frequencies (26.3 and 39.5 GHz), owing to the shorter wavelengths of the EMW, the power loss is primarily concentrated in the middle and upper regions of the honeycomb wall. Thus, the gradient structure originated from the GHCS, which endows the metamaterial with superior impedance

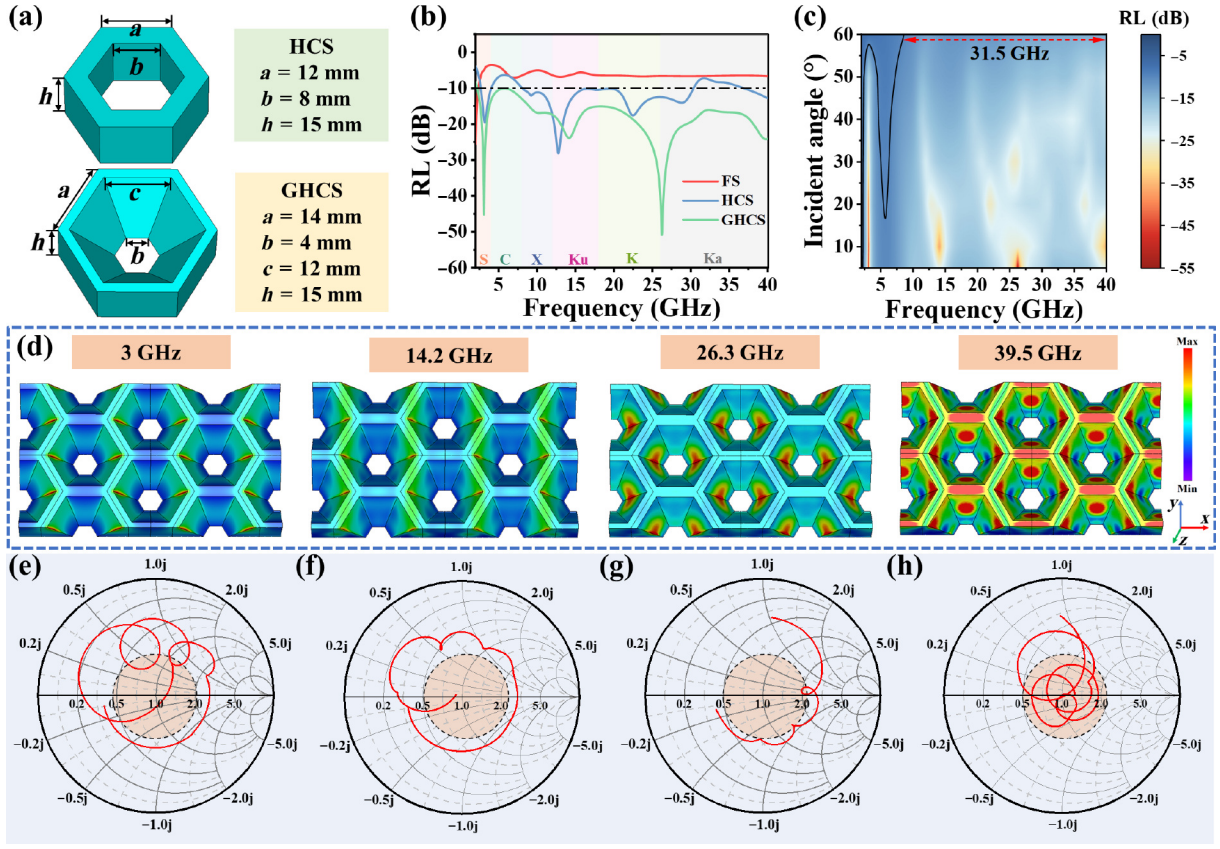

Fig. 10 (a) Schematic and structural parameters of the HCS and GHCS. (b) Simulated reflectivities of the three structures. (c) Calculated RL of the GHCSs under oblique incidence (with incident angles ranging from 5° to 60°). (d) Power loss distributions of the GHCSs at four absorption peak frequencies. Smith circle diagrams of single-layer Co_xNi_y@C and GHCSs with equal thicknesses: (e) CN1, (f) CN2, (g) CN3, and (h) GHCSs.

matching over a wide frequency range, as evidenced by the Smith circle diagram. As shown in Figs. 10(e)–10(h), the input impedance curves of a layered MOF-derived Co_xNi_y@C absorber with equal thickness are far from the perfect impedance matching region (orange area) over the entire 2–40 GHz range. In contrast, the majority input impedance curve of the GHCSs with rational structural design falls in the orange region, exhibiting approximately perfect impedance matching with free space. Thus, the simulated GHCS metamaterial is expected to be applied in lightweight and broadband EMW absorption applications.

4 Conclusions

In this study, Co_xNi_y@C composites with various Co/Ni atomic ratios were successfully fabricated via a straightforward MOF-derived strategy. The difference in work function between Co_xNi_y and C can induce a BIEF at the interface, which facilitates electron migration and leads to spatial charge separation, thereby enhancing dielectric loss through intense nanoscale interfacial polarization relaxation. Additionally, the highly dispersed CoNi nanoparticles within the nanorods strengthened the magnetic response and significantly contributed to magnetic loss. Owing to its rational 1D hierarchical nanorod architecture and synergistic electromagnetic attenuation, Co_2Ni@C exhibited superior EMW absorption performance, with an EAB of 4.9 GHz at 1.75 mm. Furthermore, by implementing a cross-scale structural design, a GHCS incorporating Co_2Ni@C realizes effective EMW absorption across 2–40 GHz at a total thickness of 15 mm. This work not only clarifies the role of the Co/Ni atomic ratio in regulating the EMW absorption performance of MOF-derived Co_xNi_y@C composites but also provides direct guidance for the cross-scale structural engineering of EMW absorption powders for practical applications.

Acknowledgements

This work was supported by the National Natural Science Foundation of China (Grant Nos. 52572051, 52231007, 52172103, and 52222204), the Jiangsu Provincial Program of Science and Technology (Grant No. BE2023044), and the Natural Science Basic Research Program in Shaanxi (Grant No. 2022JC-25).

Author contributions

Bo Huang: Writing – review & editing, Writing – original draft, Visualization, Methodology, Investigation, Formal analysis, Conceptualization. Fang Ye: Writing – review & editing, Writing – original draft, Resources, Methodology, Investigation, Formal analysis. Jingwen Deng: Investigation, Methodology. Jingchao Wang: Visualization, Methodology, Investigation. Chen Li: Writing – review & editing, Resources, Methodology. Yuchen Cao: Writing – review & editing, Methodology. Wenjing Zhang: Visualization. Xiaomeng Fan: Writing – review & editing, Validation, Supervision, Conceptualization.

Availability of data and materials

The data that support the findings of this study are available from the corresponding author upon reasonable request.

Competing interests

The authors declare that they have no known competing financial interests or personal relationships that could have appeared to influence the work reported in this paper. The author Xiaomeng Fan is the Editorial Committee member of this journal.

Electronic Supplementary Material

Supplementary material is available in the online version of this article at https://doi.org/10.26599/JAC.2025.9221224.

References

[1] Qian JJ, Ma DD, Zou YX, *et al.* Implanting Ag nanoparticles in SiOC ceramic nanospheres for exceptional electromagnetic wave absorption and antibacterial performance. *J Adv Ceram* 2025, **14**: 9221084.

[2] Liu CC, Chen QY, Sun P, *et al.* Synthesis of novel high-entropy diborides with high-efficiency electromagnetic wave absorption and excellent thermal stability. *J Adv Ceram* 2025, **14**: 9221030.

[3] Yan YF, Qin GY, Zhang KL, *et al.* Enhancing microwave absorption performance of MoS_2 by synergistic effect of Fe doping. *J Adv Ceram* 2025, **14**: 9221039.

[4] Zhang YL, Liu A, Tian YY, *et al.* Direct-ink-writing printed aerogels with dynamically reversible thermal management and tunable electromagnetic interference shielding. *Adv Mater* 2025, **37**: 2505521.

[5] Zhang YL, Wang L, Zhang JL, *et al.* Fabrication and investigation on the ultra-thin and flexible $Ti_3C_2T_x$/co-doped polyaniline electromagnetic interference shielding composite films. *Compos Sci Technol* 2019, **183**: 107833.

[6] Qian JJ, Ma DD, Zhou XL, *et al.* Synthesis of SiOC@C ceramic nanospheres with tunable electromagnetic wave absorption performance. *J Adv Ceram* 2024, **13**: 1394–1408.

[7] He MK, Zhang KY, Qiu H, *et al.* Low-frequency microwave absorption composites. *Adv Sci* 2025, **12**: e11580.

[8] Qiao LJ, Bi JQ, Liang GD, *et al.* Synthesis of high-entropy MXenes with high-efficiency electromagnetic wave absorption. *J Adv Ceram* 2023, **12**: 1902–1918.

[9] Wang ZJ, Zhang F, Wang NN, *et al.* Ternary layered boride MoAlB: A novel thermo-regulation microwave absorbing ceramic material. *J Adv Ceram* 2024, **13**: 699–710.

[10] Liu YL, Geng WZ, Wang LN, *et al.* Designing MXene hydrogels for flexible and high-efficiency electromagnetic wave absorption using digital light processing 3D printing. *Chem Eng J* 2025, **505**: 159489.

[11] Wu LH, Shi SH, Wang GZ, *et al.* Carbon nanocoils/carbon foam as the dynamically frequency-tunable microwave absorbers with an ultrawide tuning range and absorption bandwidth. *Adv Funct Mater* 2022, **32**: 2209898.

[12] Zhao L, Qian YX, Xu XF, *et al.* Thermal-insulating carbon foam for efficient electromagnetic energy absorption and conversion. *Nano Energy* 2025, **143**: 111313.

[13] Xiao JX, Zhan BB, He MK, *et al.* Interfacial polarization loss improvement induced by the hollow engineering of necklace-like PAN/carbon nanofibers for boosted microwave absorption. *Adv Funct Mater* 2025, **35**: 2316722.

[14] Qu N, Sun HX, Sun YY, *et al.* 2D/2D coupled MOF/Fe composite metamaterials enable robust ultra–broadband microwave absorption. *Nat Commun* 2024, **15**: 5642.

[15] Che RC, Peng LM, Duan XF, *et al.* Microwave absorption enhancement and complex permittivity and permeability of Fe encapsulated within carbon nanotubes. *Adv Mater* 2004, **16**: 401–405.

[16] Zeng XJ, Jiang X, Ning Y, *et al.* Construction of dual heterogeneous interface between zigzag-like Mo–MXene nanofibers and small CoNi@NC nanoparticles for electromagnetic wave absorption. *J Adv Ceram* 2023, **12**: 1562–1576.

[17] Tan DL, Wang Q, Li MR, *et al.* Magnetic media synergistic carbon fiber@Ni/NiO composites for high-efficiency electromagnetic wave absorption. *Chem Eng J* 2024, **492**: 152245.

[18] Liang QQ, He MK, Zhan BB, *et al.* Yolk-shell CoNi@N-doped carbon-CoNi@CNTs for enhanced microwave absorption, photothermal, anti-corrosion, and antimicrobial properties. *Nano-Micro Lett* 2025, **17**: 167.

[19] Han YX, Guo H, Qiu H, *et al.* Multimechanism decoupling for low-frequency microwave absorption hierarchical Fe-doped co magnetic microchains. *Adv Funct Mater* 2025, **35**: 2506803.

[20] Guo ZQ, Lan D, Zhang CH, *et al.* "Two birds one stone" strategy to integrate electromagnetic wave absorption and self-anticorrosion in magnetic nanocomposites with double-shell hollow structure. *J Mater Sci Technol* 2025, **220**: 307–319.

[21] Huang MQ, Li BX, Qian YT, *et al.* MOFs-derived strategy and ternary alloys regulation in flower-like magnetic-carbon microspheres with broadband electromagnetic wave absorption. *Nano-Micro Lett* 2024, **16**: 245.

[22] Wang BL, Ding MC, Shao CX, *et al.* Facile synthesis of Co_xFe_y@C nanocomposite fibers derived from pyrolysis of cobalt/iron chelate nanowires for strong broadband electromagnetic wave absorption. *Chem Eng J* 2023, **465**: 142803.

[23] Zhang Y, Yang SH, Xin Y, *et al.* Designing symmetric gradient honeycomb structures with carbon-coated iron-based composites for high-efficiency microwave absorption. *Nano-Micro Lett* 2024, **16**: 234.

[24] Zhang SS, Liu GZ, Lv SH, *et al.* Ti-MOF@Metal-polyphenol network derived $TiN_{0.9}$@NC/magnetic MWCNTs composites for microwave absorption. *Chem Eng J* 2023, **468**: 143763.

[25] Wang L, Huang MQ, Yu XF, *et al.* MOF-derived $Ni_{1-x}Co_x$@Carbon with tunable nano–microstructure as lightweight and highly efficient electromagnetic wave absorber. *Nano-Micro Lett* 2020, **12**: 150.

[26] Qin L, Liu S, Qin SH, *et al.* MOF derived porous Ni/Co@C nanocomposite as electromagnetic wave absorber with optimized impedance matching. *Compos Commun* 2022, **33**: 101196.

[27] Liu QH, Xu XH, Xia WX, *et al.* Dependency of magnetic microwave absorption on surface architecture of $Co_{20}Ni_{80}$ hierarchical structures studied by electron holography. *Nanoscale* 2015, **7**: 1736–1743.

[28] Ge JW, Cui Y, Qian JX, *et al.* Morphology-controlled CoNi/C hybrids with bifunctions of efficient anti-corrosion and microwave absorption. *J Mater Sci Technol* 2022, **102**: 24–35.

[29] Yu YD, Fang Y, Hu Q, *et al.* Hollow MOF-derived CoNi/C composites as effective electromagnetic absorbers in the X-band and Ku-band. *J Mater Chem C* 2022, **10**: 983–993.

[30] Liu C, Qiao J, Zhang X, *et al.* Bimetallic MOF-derived porous CoNi/C nanocomposites with ultra-wide band microwave absorption properties. *New J Chem* 2019, **43**: 16546–16554.

[31] Xie H, Li JM, Yang R, *et al.* Controllable fabrication of CoNi bimetallic alloy for high-performance electromagnetic wave absorption. *RSC Adv* 2024, **14**: 9791–9797.

[32] Wang YL, Yang SH, Wang HY, *et al.* Hollow porous CoNi/C composite nanomaterials derived from MOFs for efficient and lightweight electromagnetic wave absorber. *Carbon* 2020, **167**: 485–494.

[33] Zhang SJ, Zheng JJ, Zhao ZW, *et al.* New prospects in built-in electric fields for electromagnetic wave absorption: From fundamentals to interdisciplinary applications. *Adv Funct Mater* 2025: 13762.

[34] Chen YK, Wang XQ, Cui WG, *et al.* Multiple Schottky contacts motivated via defects to tune the response ability of electromagnetic waves. *Adv Funct Mater* 2025, **35**: 2417215.

[35] Zhou Q, Shi TT, Xue B, *et al.* Multi-scale integrated design and fabrication of ultra-broadband electromagnetic absorption utilizing multi-walled carbon nanotubes-based hierarchical metamaterial. *Compos Sci Technol* 2023, **232**: 109877.

[36] Yu ZJ, Chen T, Du HZ, *et al.* Single-source-precursor derived SiOC ceramics with *in-situ* formed CNTs and core–shell structured CoSi@C nanoparticles towards excellent electromagnetic wave absorption properties. *J Adv Ceram* 2023, **12**: 1119–1135.

[37] Niu HH, Tu XY, Zhang S, *et al.* Engineered core-shell SiO_2@$Ti_3C_2T_x$ composites: Towards ultra-thin electromagnetic wave absorption materials. *Chem Eng J* 2022, **446**: 137260.

[38] Huang B, Ye F, Liu YQ, *et al.* Thin and ultra-broadband electromagnetic absorption carbonyl iron-based metamaterial *via* multiscale synergic dielectric-magnetic design. *Compos Sci Technol* 2024, **250**: 110509.

[39] Wu LH, Liu J, Liu X, *et al.* Microwave-absorbing foams with adjustable absorption frequency and structural coloration. *Nano Lett* 2024, **24**: 3369–3377.

[40] Huang B, Cao YC, Ye F, *et al.* Multiscale synergistic design of SiC_f/SiBCN-based metamaterial for high-performance electromagnetic wave absorption in a wide temperature domain. *J Mater Sci Technol* 2026, **249**: 203–213.
[41] Wang QB, Luo JH, Wu YH, *et al.* Tunable electromagnetic response behaviors via cross-scale morphological structural engineering for ultra-wideband microwave absorption. *Chin J Chem* 2025, **43**: 2756–2770.
[42] Cao YC, Ye F, Liang J, *et al.* Structural-functional-integrated ultra-wideband microwave-absorbing composites based on *in situ*-grown graphene meta-nanointerface. *Adv Funct Mater* 2024, **34**: 2411271.
[43] Liang J, Ye F, Song Q, *et al.* In-plane heterogeneous structure-boosted interfacial polarization in graphene for wide-band and wide-temperature microwave absorption. *Chem Eng J* 2024, **497**: 154307.
[44] Huang B, Ye F, Cao YC, *et al.* Hierarchical CoNi@C microspheres assembled by high-content CoNi nanoparticles interpenetrated into amorphous carbon for high-performance electromagnetic wave absorption. *J Mater Sci Technol* 2026, **253**: 1–11.
[45] Wu NN, Xu DM, Wang Z, *et al.* Achieving superior electromagnetic wave absorbers through the novel metal–organic frameworks derived magnetic porous carbon nanorods. *Carbon* 2019, **145**: 433–444.
[46] Xiang Z, Song YM, Xiong J, *et al.* Enhanced electromagnetic wave absorption of nanoporous Fe_3O_4@carbon composites derived from metal-organic frameworks. *Carbon* 2019, **142**: 20–31.
[47] Pan F, Liu ZC, Deng BW, *et al.* Magnetic Fe_3S_4 LTMCs micro-flowers@wax gourd aerogel-derived carbon hybrids as efficient and sustainable electromagnetic absorber. *Carbon* 2021, **179**: 554–565.
[48] Cheng JB, Zhao HB, Zhang AN, *et al.* Porous carbon/Fe composites from waste fabric for high-efficiency electromagnetic wave absorption. *J Mater Sci Technol* 2022, **126**: 266–274.
[49] Yang ZT, Wang T, Wang JF, *et al.* Heterogeneous N-doped carbon composite $NiSe_2$–FeSe double-shell hollow nanorods for tunable and high-efficient microwave attenuation. *Carbon* 2023, **201**: 491–503.
[50] Chen JB, Zheng J, Huang QQ, *et al.* Enhanced microwave absorbing ability of carbon fibers with embedded FeCo/$CoFe_2O_4$ nanoparticles. *ACS Appl Mater Inter* 2021, **13**: 36182–36189.
[51] Li X, Yu LZ, Xiang Z, *et al.* Enhanced electromagnetic wave absorption of olive-like Fe_3O_4/Fe@C core-shell nanocomposite in Ku band. *J Alloys Compd* 2020, **821**: 153275.
[52] Chen F, Zhang SS, Guo RD, *et al.* 1D magnetic nitrogen doped carbon-based fibers derived from NiFe Prussian blue analogues embedded polyacrylonitrile via electrospinning with tunable microwave absorption. *Compos Part B Eng* 2021, **224**: 109161.
[53] Jin C, Wu ZC, Zhang RX, *et al.* 1D electromagnetic-gradient hierarchical carbon microtube *via* coaxial electrospinning design for enhanced microwave absorption. *ACS Appl Mater Inter* 2021, **13**: 15939–15949.
[54] Lü YY, Wang YT, Li HL, *et al.* MOF-derived porous Co/C nanocomposites with excellent electromagnetic wave absorption properties. *ACS Appl Mater Inter* 2015, **7**: 13604–13611.
[55] Lin J, Wen HL, Feng ZB, *et al.* Anion injection in dielectric ecosystems to construct dual built-in electric fields for efficient electromagnetic response. *Adv Funct Mater* 2025, **35**: 2505381.
[56] Song XJ, Han Y, Wang X, *et al.* First-principles study of adhesion strength and stability of the TiB_2/TiC interface in composite materials. *Ceram Int* 2018, **44**: 1756–1763.
[57] Jiang B, Yang W, Wang CN, *et al.* Lightweight porous cobalt-encapsulated nitrogen-doped carbon nanotubes for tunable, efficient and stable electromagnetic waves absorption. *Carbon* 2023, **202**: 173–186.
[58] Luo H, Lv SH, Liu GZ, *et al.* Multi-interfacial magnetic carbon nanotubes encapsulated hydrangea-like NiMo/MoC/N-doped carbon composites for efficient microwave absorption. *Carbon* 2022, **196**: 828–839.
[59] Sun H, Che RC, You X, *et al.* Cross-stacking aligned carbon-nanotube films to tune microwave absorption frequencies and increase absorption intensities. *Adv Mater* 2014, **26**: 8120–8125.
[60] Zhang S, Li MR, Chen GN, *et al.* Achieving high performance microwave attenuation by anchoring magnetic CoNi nanoparticles onto few-layer $Ti_3C_2T_x$MXene. *J Alloys Compd* 2025, **1023**: 180015.
[61] Song LM, Hu FY, Chen YQ, *et al.* Heterointerface-engineered SiC@SiO_2@C nanofibers for simultaneous microwave absorption and corrosion resistance. *Adv Sci* 2025, **12**: 09071.
[62] Tian ZH, Hu FY, Zhang PG, *et al.* High-entropy engineering of A-site in MAX phases toward superior microwave absorption properties. *Matter* 2025, **8**: 102367.